Modelling the role of cytotoxic T lymphocytes in tumour regression

Beck, R.J.

Chapter 5

Quantification of T cell exhaustion in B16F10 melanoma through mathematical modeling

Richard J Beck[1], Sander Sloot[1], Hirokazu Matsushita[2], Kazuhiro Kakimi[2], Joost B Beltman[1]

1. **Division of Drug Discovery and Safety, Leiden Academic Centre for Drug Research, Leiden University, Leiden, The Netherlands**
2. **Department of Immunotherapeutics, The University of Tokyo Hospital, Tokyo, Japan**

Abstract

Cytotoxic T Lymphocytes (CTLs) are an important component of the adaptive immune response and have an important role in controlling tumours. Improved understanding of CTL interactions within solid tumours will yield insights of benefit to the development of immunotherapeutic strategies against cancer. CTLs are best known for their ability to lyse antigen presenting targets, however they also secrete cytokines such as interferon-γ (IFN-γ), which can inhibit cell cycle progression and thus block proliferation of neighbouring cells. In this study, we take a systems biology approach to compare the importance of cytolytic versus IFN-γ mediated cytostatic effects in a murine melanoma model. We integrated measurements of tumour volume, fluorescent imaging data, and transcriptomics data to inform an ordinary differential equation (ODE) model of CTL activities inside the tumour. Our model predicted that the cytotoxic effects of CTLs were very small, and that the cytostatic effects of IFN-γ were likely responsible for almost all of the observed difference in tumour growth between the CTL treated versus the untreated tumours. Moreover, our analysis and subsequent modelling revealed that the window of IFN-γ production was much shorter than the period of CTLs infiltrating the tumour. This was consistent with the dynamics of delayed upregulation of CTL exhaustion markers TIM-3 and LAG-3 but not with the dynamics of PD-1 and PD-L1. This suggests that within B16F10 melanomas TIM-3 and LAG-3 have a more important role than the PD-1/PD-L1 axis in the development of a dysfunctional CTL phenotype, especially at late stages of anti-tumour T cell responses.

Introduction

Immunotherapy is an emerging strategy for treatment of cancer, with an ever growing number of immunotherapies having reached clinical trials or been approved already[1]. Blood cancers were amongst the first to be successfully treated with immunotherapy[2]; to date solid tumours have proved more challenging. Despite this, several treatments are already available for solid tumours and many more are under trial[3]. Although there has been some success with immunotherapy so far, there is a pressing need for greater mechanistic understanding of the interactions of immune cells within solid tumours. Such understanding may help expand the scope of immunotherapies to different cancers, identify biomarkers to predict which patients might benefit from immunotherapy[4], optimise the dosing schedule for immunotherapies[5,6], or identify potential combination therapeutic strategies[7]. Mathematical or computational models are a useful tool to develop such understanding, since they can link data from different sources and make quantitative predictions for what we should expect under different conditions.

$CD8^+$ Cytotoxic T Lymphocytes (CTLs) are a key player in the anti-cancer immune response, and many immunotherapy strategies are focussed on these cells. Two prominent examples are blockade of inhibitory receptors such as PD-1 expressed on CTLs in hopes of “removing the brakes” on the immune response[8,9], or adoptive transfer of engineered (CAR) T Cells[10,11]. Therefore understanding the functioning of CTLs inside tumours is of foundational importance for the rational design of immunotherapies. Secretion of the cytokine IFN-γ is a hallmark of activated CTLs, yet due to its pleiotropic effects the exact effects of this cytokine in solid tumours remain poorly understood. Indeed, some have even noted the “paradoxical” role of IFN-γ in tumour progression[12], paradoxical in the sense that IFN-γ can have both pro-tumour and anti-tumour effects. Amongst the pro-tumour effects, IFN-γ can lead to recruitment of suppressive cells such as regulatory T cells or myeloid derived suppressor cells (MDSCs), or can induce expression of immune checkpoint ligands such as PD-L1 on tumour cells[13,14]. Amongst the anti-tumour effects, IFN-γ can aid in the recruitment of innate immune effectors, kill tumour cells, or exert antiproliferative effects on tumour cells[15–17].

Here, we focus on the antiproliferative effects IFN-γ has on tumour cells. The antiproliferative effects are mediated by inhibitors of cyclin dependent kinases which result in arrest of tumour cells at the G_1 phase of the cell cycle, which has been shown in a variety of cell lines[15–17]. However, IFN-γ also has anti-angiogenic effects which may in part explain the reduction in tumour cell proliferation. Previously we have used computational models to demonstrate how an antiproliferative effect mediated by cytokines could have a very potent effect on tumour progression, since through cytokine signalling CTLs can control many tumour cells, thus stalling tumour growth and buying time for killing of tumour cells by CTLs [18,19]. However, in our previous modeling work no direct data linking the proliferation of tumour cells to IFN-γ levels inside the tumours was available. Therefore, here we have used data from another study by Matshushita and coworkers where the antiproliferative effects of IFN-γ were explicitly explored[15]. In that study, CTLs strongly inhibited B16F10 melanoma tumour growth, but this effect was reversed when adoptive T cell transfer was accompanied by administration of anti-IFN-γ antibodies. In

addition, histological analysis of tumours expressing a cell cycle sensor revealed that most cells were arrested in the G_1-phase after CTL transfer.

In the current study we sought to gain a quantitative understanding of the role of IFN-γ mediated antiproliferative effects, hence we specifically quantified how important were the effects of IFN-γ in tumour control relative to the canonical killing functions of CTLs. To answer that question, we developed an Ordinary Differential Equation model which integrated data from Matshushita et al.[15] to arrive at a coherent, quantitative description of the intratumoural activities of CTLs and their interactions with the tumour following adoptive transfer. Consistent with our previous study of B16F10 tumours[19], our model predicted that the cytotoxic effects of CTLs were very small, and that the cytostatic effects of IFN-γ were responsible for almost all of the observed difference in tumour growth between the CTL treated versus the untreated tumours. Moreover, our analysis and subsequent modelling indicated that the window of IFN-γ production was very short, with CTLs losing the ability to produce IFN-γ within a few days of CTLs infiltrating the tumour. Markers of CTL exhaustion such as TIM-3 and LAG-3 were still increasing over this period, suggesting that CTLs had become exhausted inside the tumour. In contrast to TIM-3 and LAG-3, the dynamics of PD-1 and PD-L1 did not coincide with the dynamics of CTL exhaustion, suggesting a relatively minor role for these checkpoints as determinants of CTL exhaustion in the B16F10 melanoma model, at least at late stages of anti-tumour immune responses.

Results

Presence of CTLs correlates with cell cycle arrest in tumour cells

Previously, the adoptive transfer of CTLs was shown to induce G1-phase cell cycle arrest of B16F10 tumour cells in an IFN-γ dependent manner[15], however the temporal evolution of this arrested state and correlation with the number of tumour infiltrating CTLs was not explicitly quantified. Therefore, we exploited previously unquantified images from the same study, taken at multiple time points after CTL transfer, to estimate the number of tumour infiltrating CTLs and B16F10 tumour nuclei. Moreover, due to the incorporated Fucci cell cycle sensor it was also possible to discriminate between B16F10 nuclei in the G1-phase and nuclei that were in other (S-G_2-M) phases of the cell cycle. In order to quantify the number of B16F10 nuclei in either the G_1 phase or in the S-G_2-M phases at different timepoints after CTL transfer, we developed automated pipelines using the ilastik[20] cell density estimation tool (see Methods). Comparison of the ilastik predictions for small subregions of sample images (Fig. 1A) selected across different time points to our own manual counts made for the same images demonstrated that our pipeline was reliable (Fig. 1B). Moreover, our estimated densities of G_1 phase (Fig. 1C) or S-G_2-M phase (Fig. 1D) on day 3 were comparable to those in the study of Matsushita et. al[15], as were the ratios of cells in G_1:S-G_2-M phases (Fig. 1E). The number of CTLs per slide was far more difficult to determine automatically, which was likely due to the irregular morphology of the CTLs and their lack of a visible nucleus. Since the number of CTLs was much lower than the number of B16F10 nuclei, we instead performed a manual count of the number of CTLs across all images (Fig.1F). We found a strong negative correlation between the number of CTLs and the G_1:S-G_2-M ratio in the sample images (Fig. 1G), with a Pearson's correlation coefficient of -0.60 (95% confidence

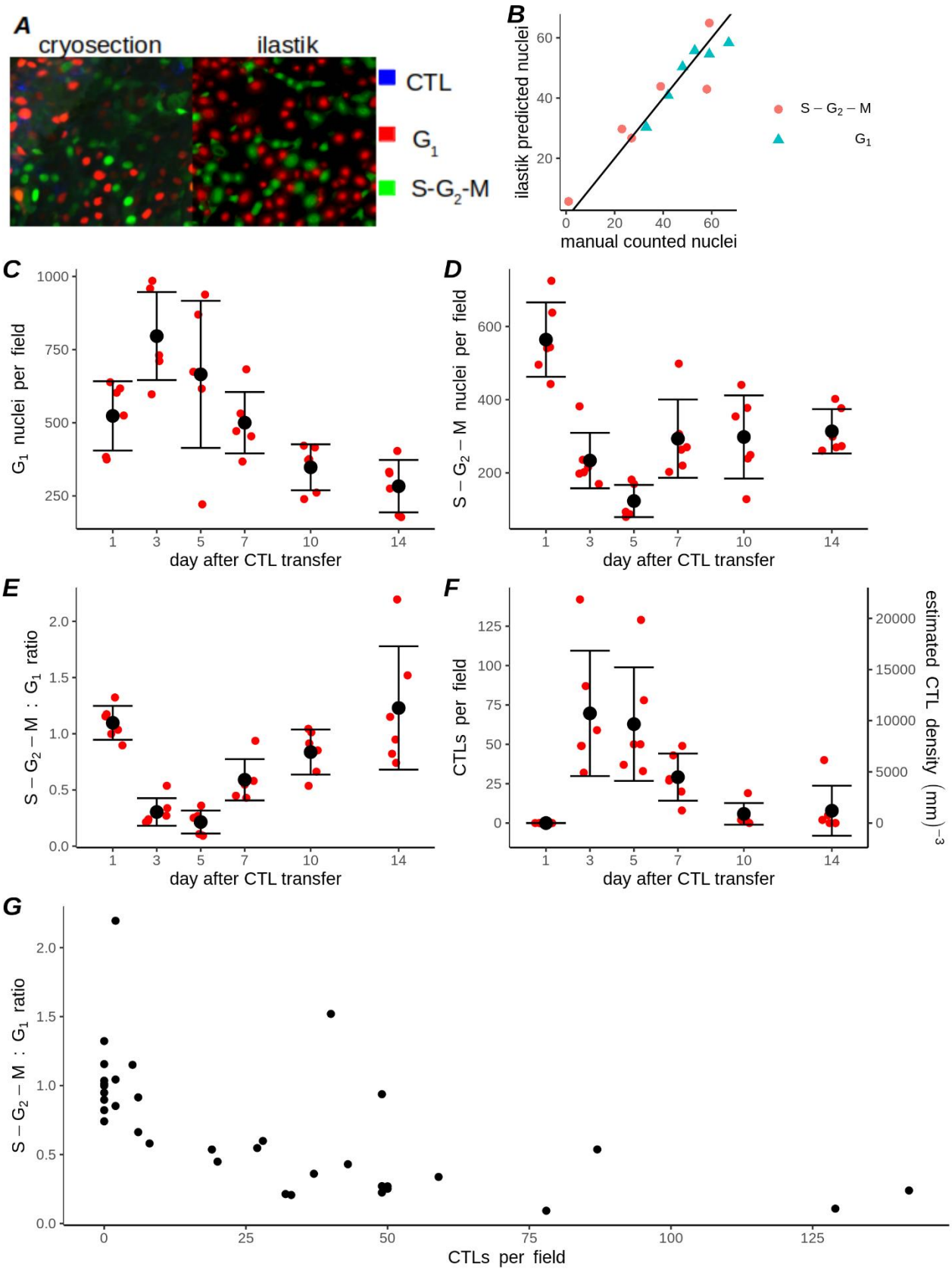
A
cryosection
ilastik
CTL
G1
S-G2-M
B
ilastik predicted nuclei
manual counted nuclei
S – G2 – M
G1
C
G1 nuclei per field
day after CTL transfer
D
S – G2 – M nuclei per field
day after CTL transfer
E
S – G2 – M : G1 ratio
day after CTL transfer
F
CTLs per field
estimated CTL density (mm)−3
day after CTL transfer
G
S – G2 – M : G1 ratio
CTLs per field

Figure 1. (displayed on previous page) Dynamics of tumour cell cycle arrest correlates closely with CTL presence. A) Comparison of cryosection image (left), with probabilities predicted by ilastik (right). G_1 and S-G_2-M phase nuclei are shown (respectively) in red or green. CTLs appear blue in the cryosection image and were not quantified using ilastik. Image shown is an example of a subregion (175x175μm) of one complete cryosection (750x550μm), which was used for training the classifier. B) Number of nuclei in cryosection subregions used for training the classifier, comparing manually counted (horizontal axis) nuclei with the ilastik estimate (vertical axis). C-D) Results of automated quantification of the number of B16F10 nuclei in the G_1 phase (C) or in the S-G_2-M phases (D), applied to the full set of cryosection images. E) Ratio of cells in S-G_2-M:G_1 phases determined from the automated density estimation results (shown in C-D). F) Number of CTLs manually counted in each cryosection. Each small red point in C-F represents the total number of cells counted per cryosection, large black points and error bars are (respectively) mean +/- standard deviation. G) Comparison of the number of CTLs (horizontal axis) with the tumour cell S-G_2-M:G_1 ratio (vertical axis) for each available fluorescent image.

interval between -0.7757570 and -0.3289711) allowing us to reject the null hypothesis of no correlation (p=0.00015). In summary, the G_1 cell cycle arrest following CTL transfer lasted for up to 5 days and its temporal dynamics were closely linked to the presence of CTLs inside the tumour.

Tumour cell cycle arrest correlates with tumour growth reduction

To check if the temporary G_1 cell cycle arrest was consistent with tumour volume progression, we also incorporated tumour volume measurements into our analysis. An exponential model of tumour growth was sufficient to describe tumour progression over the studied interval (Fig. 2A), i.e. within the observed range of tumour sizes there was not yet any indication for a potential carrying capacity limiting tumour growth. Volume estimates were available from three separate experiments with CTL treatment (Fig. 2B). We noted some minor yet apparent systematic differences between experiments. For instance, almost all volumes recorded on day -1 were larger in one of the biological replicates (compare red and green points in Fig. 2A-B, day -1). Despite these minor discrepancies, the broad pattern of tumour progression was similar across replicates, with substantially arrested growth between days 3-7. Nevertheless, such systematic differences between experiments could potentially distort our results, for example because the switching from 12 mice to 2 mice between measurements going from days 7-10 (Fig. 2B) would artificially introduce a period of tumour growth above even the untreated growth rate into our data. To avoid this issue, we converted the data into estimates of the tumour growth rate between measurement intervals for both the data without CTL transfer (Fig. 2C) and those with CTL transfer (Fig. 2D). For the experiments where CTLs were transferred, this resulted in consistent values between experiments and allowed us to safely incorporate the additional measurements from the 2 mice that were recorded up until day 14. From this analysis, reduced tumour growth was apparent between days 3-7 (Fig. 2D; points centred on days 4 and 6), but growth recovery in the measurement interval between days 7-10 (Fig. 2D; point centred on day 8.5). Therefore the period of tumour growth reduction was coincident with the period of G_1 phase tumour cell cycle arrest (Fig. 1E), and by extension also coincident with the presence of CTLs within the tumour (Fig. 1F).

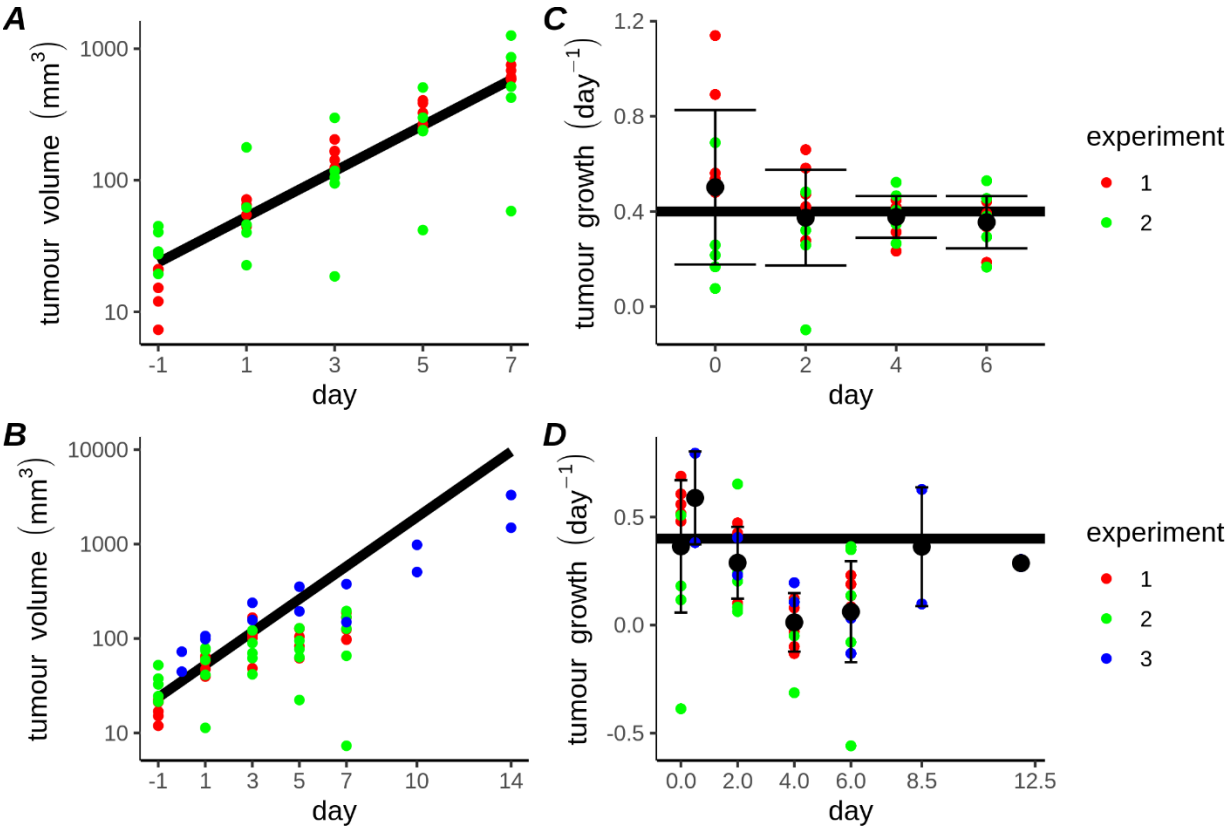

Figure 2. Tumour volume dynamics corresponds to G_1 cell cycle arrest and CTL presence. A) Tumour volume progression from 2 different experiments (n=5 mice per experiment) without CTL treatment. B) Tumour volume progression from 3 different experiments (n=5 mice in experiments 1&2, n=2 mice in experiment 3) with CTLs transferred on day 0. C) Untreated tumour growth rate estimates for each mouse taken across each of the measurement intervals shown in A. D) Tumour growth rate estimates for each mouse receiving CTL transfer on day 0. Solid black lines in A-D show results of fitting an exponential growth model ($g=0.4\ day^{-1}$) to the untreated data (A,C) and are shown alongside CTL treated data (B,D) for comparison. Black points and error bars in C-D represent (respectively) mean +/- standard deviation of all points. Points in C-D are shown at the midpoint of the interval over which they were estimated. Coloured dots in all panels indicate the independent experiments consisting of multiple mice.

Loss of IFN-γ production precedes loss of CTLs from tumours

IFN-γ secreted by CTLs was the putative agent which led to cell cycle arrest and the transient reduction of tumour progression in our studied data[15]. As a proxy for IFN-γ levels inside the tumour we used mRNA expression data recorded within the same experiments as the previously analysed image (Fig. 1) and volume progression data (Fig. 2). We found that Cd8a transcription dynamics (Fig.3A row 1) matched the CTL dynamics measured in the images (Fig. 1F), indicating agreement between the transcriptomics data and the imaging data with respect to CTL abundance. However, the dynamics of IFN-γ transcription appeared much different to those of the CTLs (Fig.3A, row 2). IFN-γ transcription peaked sharply on day 3 after CTL transfer, but had dropped sharply by day 5 and returned to basal levels on day 7, when CTLs still remained inside the tumour. To verify the dynamics of IFN-γ, we also checked Stat1 and Socs1 (Fig 3A, rows 3-

4) which are downstream of the IFN-γ receptor[21] in the IFN-γ signalling pathway. These followed very similar dynamics to IFN-γ mRNA, lending support to the idea that the IFN-γ mRNA expression data was a suitable proxy for IFN-γ signalling dynamics inside the tumour.

We hypothesized that the difference in dynamics between CTLs and IFN-γ transcription was due to a gradual CTL exhaustion inside the tumour, leading to a loss of their effector functions. Exhausted T Cells display hierarchical loss of effector functions including secretion of cytokines such as proliferative ability, capacity to kill target cells, and secretion of IFN-γ[22,23]. Several genes are associated with the exhausted T Cell state[24,25], and as T Cells become progressively more exhausted they express a greater diversity of inhibitory receptors[23]. Indeed, we could identify transcripts for a number of well described immune checkpoint molecules in the mRNA dataset, including PD1, its ligand PD-L1, LAG-3, and TIM-3 (Fig. 3B). Overall, our analysis suggests that the pulse of IFN-γ transcription remains brief despite CTLs still being present within the tumour and is due to development of an exhausted phenotype amongst the transferred CTLs.

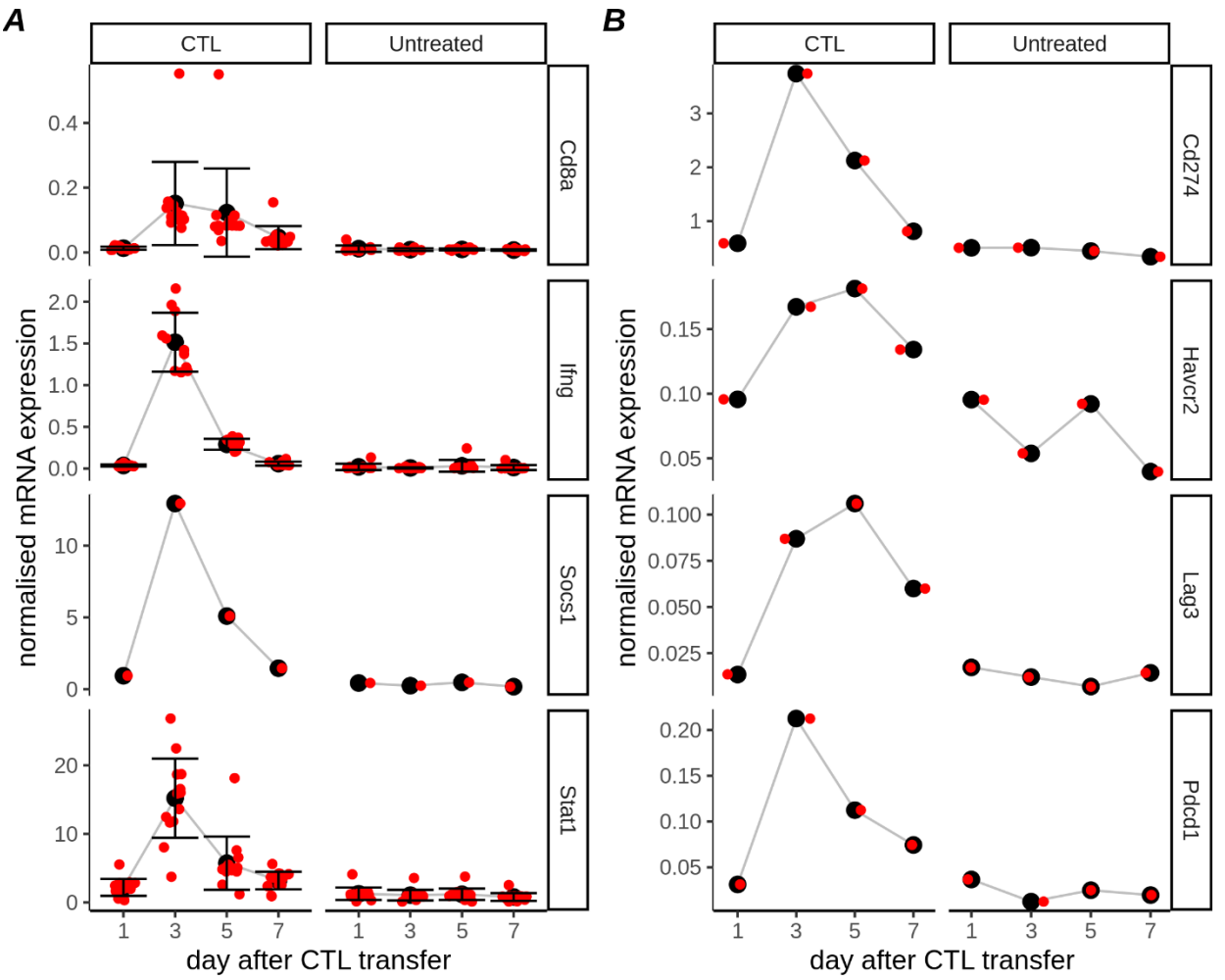

Figure 3. Dynamics of selected genes from microarray dataset. A) Comparison of dynamics of probes specific for Cd8a (row1), Ifng (row 2), Socs1 (row 3), or Stat1 (row 4) between CTL treated and untreated mice (across columns). Black points and error bars in A represent (respectively) mean +/- s.d for all probes

at a given time point. B) Comparison of dynamics of probes specific for mRNA coding PD-1 (Pdcd1) and PD-L1 (Cd274), TIM-3 (Havcr2) and LAG-3 (Lag3) (along rows), between CTL treated and untreated mice (across columns). Red points in A-B represent expression values after normalisation at the 75th percentile.

IFN-γ transcription dynamics are compatible with G_1 phase tumour cell cycle arrest

Due to the early reduction in IFN-γ signalling, it is unclear whether IFN-γ can be entirely responsible for the G_1 phase tumour cell cycle arrest which followed highly similar dynamics to the CTLs. To test the compatibility of the IFN-γ transcription data with the dynamics of the CTLs and the tumour cell cycle dynamics, we developed an ODE model. Our ODE model describing the interactions between CTLs and the tumour (Fig. 4A) features an explicit description of the cell cycle of tumour cells, in which they cycle from G_1 phase into S-G_2-M phases at rate k_{gs}, and then back into G_1 phase at rate k_{sg}. The model also features CTLs which kill tumour cells at rate k_e and produce IFN-γ, which precludes tumour cells from transferring from G1 phase to S phase. The sensitivity of tumour cell cycle arrest to IFN-γ is determined by the parameter k_i. To test the contribution of the two CTL effector functions to tumour control (i.e., killing and antiproliferative effect), we linearly interpolated between the experimental data for the number of CTLs (Fig. 4B) and for IFN-γ expression (Fig. 4C), and used these interpolations directly as inputs to our model. Subsequently, we tested different combinations of the parameters k_e and k_i (Fig. 4D) to find the best fit to the tumour growth rate (Fig. 4E, red line) and the S-G_2-M : G_1 ratios (Fig. 4F, red line) determined from the experimental data. Our best fitting parameter set (Fig. 4D; marked with black circle) had a value of k_e=1 (CTL^{-1} day^{-1}) although other values for k_e in the range 0-3 (CTL^{-1} day^{-1}) led to relatively low errors, consistent with killing rates we have previously estimated for CTLs against B16F10 melanoma tumours[19]. The best fitting value for the antiproliferative effect (k_i=8.5 IFN^{-1} mm^3) led to sharp reductions in the transition rate of tumour cells out of the G_1 phase for the IFN-γ expression levels found in our data (Fig. 4G). At the peak of IFN-γ expression on day 3, the transition rate from G_1 to S-G_2-M phases (k_{gs}) was reduced to 7% of its original value, and even at the lower IFN-γ expression levels measured on other days k_{gs} was significantly reduced (Figs. 4C, 4G; dashed lines). Thus our best fitting parameters implied that cycling tumour cells are sensitive to IFN-γ even at low expression levels. When we took the best fitting parameters and disabled killing by setting k_e=0 (Fig. 4D; marked with black square), most of the tumour growth reduction was preserved (Fig. 4E, blue dashed line). In contrast, taking our best fitting parameters and disabling the antiproliferative effect of IFN-γ (Fig. 4D; marked with triangle) resulted in only a very small reduction in the net growth rate of the tumours (Fig. 4E, green dashed line). Overall, these results support our previous analysis showing that an antiproliferative effect of IFN-γ is more important than CTL cytotoxicity to control B16F10 tumours[19]. Moreover, these results show that the dynamics of IFN-γ are compatible with the dynamics of the tumour cell cycle arrest, despite the apparently short duration of IFN-γ production.

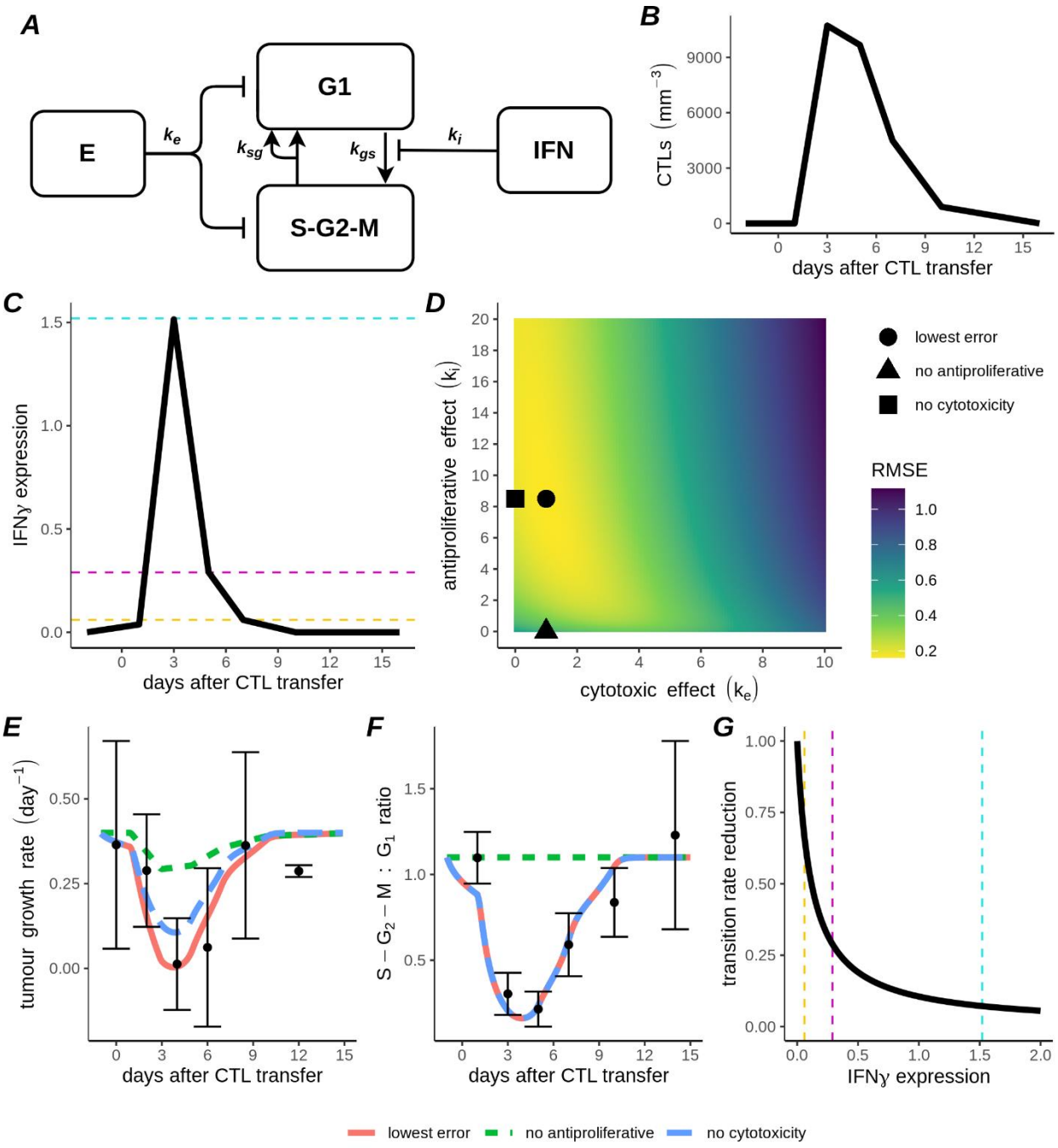

Figure 4. Compatibility of IFN-γ transcription dynamics with tumour cell cycle arrest. A) Schematic for ODE model to compare CTL killing and IFN-γ mediated antiproliferative effect in B16F10 melanoma. B-C) Linear interpolation of mean CTL density (B) and mean IFN-γ expression (C). D) Heatmap showing root-mean-square error (RMSE) for different combinations of the CTL killing rate parameter (k_e) and the parameter controlling the sensitivity of cell-cycle arrest to IFN-γ (k_i). E-F) Predictions for tumour growth rate (E) and ratio of tumour cells in S-G_2-M : G_1 states (F) for the combination of parameters with the lowest RMSE (solid red line). In addition, simulations are shown with either the best fitting k_i parameter and k_e=0 (blue long dashed line), or with the best fitting k_e parameter and k_i=0 (green short dashed line). G) Fractional reduction in transition rate from G_1 to S-G_2-M phase with varying IFN-γ expression levels, for the best-fitting

parameter value k_i=8.5 IFN^{-1} mm^3. Dashed lines in C and G highlight the predicted reduction in transition rate from G_1 to S-G_2-M phase for the mean IFN-γ expression levels measured on days 3 (cyan),5 (magenta) and 7 (yellow).

CTL exhaustion quantitatively explains IFN-γ transcription dynamics

In order to explain the dynamics of CTLs and IFN-γ and to quantify the importance of different immune checkpoints in these dynamics, we extended our ODE model (Fig. 5A). In this extended model, CTLs infiltrate the tumour at a basal rate s_0 , expand within the tumour at rate s_e, and die with rate d_e. In addition to their killing of tumour cells, CTLs inside the tumour produce IFN-γ. Finally our model includes the immune checkpoints LAG-3, TIM-3, PD1, and its ligand PDL1, which decrease the activity of CTLs (see Methods). We fit this ODE model simultaneously to all the experimental data discussed in Figures 1-3, using Min-Max feature scaling to surmount the issue of comparing measurements from different modalities (see Methods), which resulted in an excellent model fit (Fig. 5B-C, magenta lines). Importantly, without using any checkpoints, we could not obtain a good fit to any of the experimental measurements (Fig. 5B, red lines), demonstrating that T cell exhaustion is required to explain the T cell anti-tumour response.

In order to identify which of the identified immune checkpoint (IC) molecules is the most important determinant of the exhausted CTL state in the *in vivo* experimental setting with B16F10 tumours, we tried fitting our model with each IC separately. Including only PD1-PDL1 as an inhibitor (green lines; Fig. 5B-C), the fits improved compared to our model with no ICs, however we were still not able to achieve a good fit to the number of CTLs counted inside the tumour, nor to the dynamics of PD-1 and PD-L1 themselves. We achieved equally good fits with LAG-3 (Fig 5B-C, dark blue lines), with TIM-3 (Fig. 5B-C, cyan lines), and with the combination model including all checkpoints together (Fig 5B-C, magenta lines). Note that these model variants gave similar predictions to the simplified model, where CTLs and IFN-γ were used as inputs to the model, in terms of the relative importance of cytotoxic effects versus antiproliferative effects (Fig. S1). We also examined the dynamics of the exhausted state, comparing the level of exhaustion for each inhibitor (Fig. 5D). When fit individually, exhaustion due to LAG-3 increased throughout the simulated period (Fig. 5D, row 1); for TIM-3, exhaustion (Fig. 5D, row 3) increased and then remained constant from day 5 until the end of the simulated period; and for PD-1/PD-L1, exhaustion peaked on day 5 and then declined afterwards (Fig, 5D, row 2). We also investigated how much the individual ICs contributed to the evolution of CTL exhaustedness for models fit with all inhibitors simultaneously, which resulted in similar exhaustion dynamics for each IC as when they were fit individually (Fig. 5E). However, the relative contributions of each individual inhibitor to the overall exhausted state was clearly different. For the best fitting parameter set (Fig. 5E, row 1), the contributions of TIM-3 and PD-1/PD-L1 towards exhaustion became negligible compared to that of LAG-3, which we verified by removing each IC individually from this best fitting parameter set (Fig. 5F, column 1). Compared to the situation with all ICs in place the model dynamics were virtually unaffected by knockout of PD-1/PD-L1 or TIM-3, whilst knockout of LAG-3 completely disrupted the model dynamics.

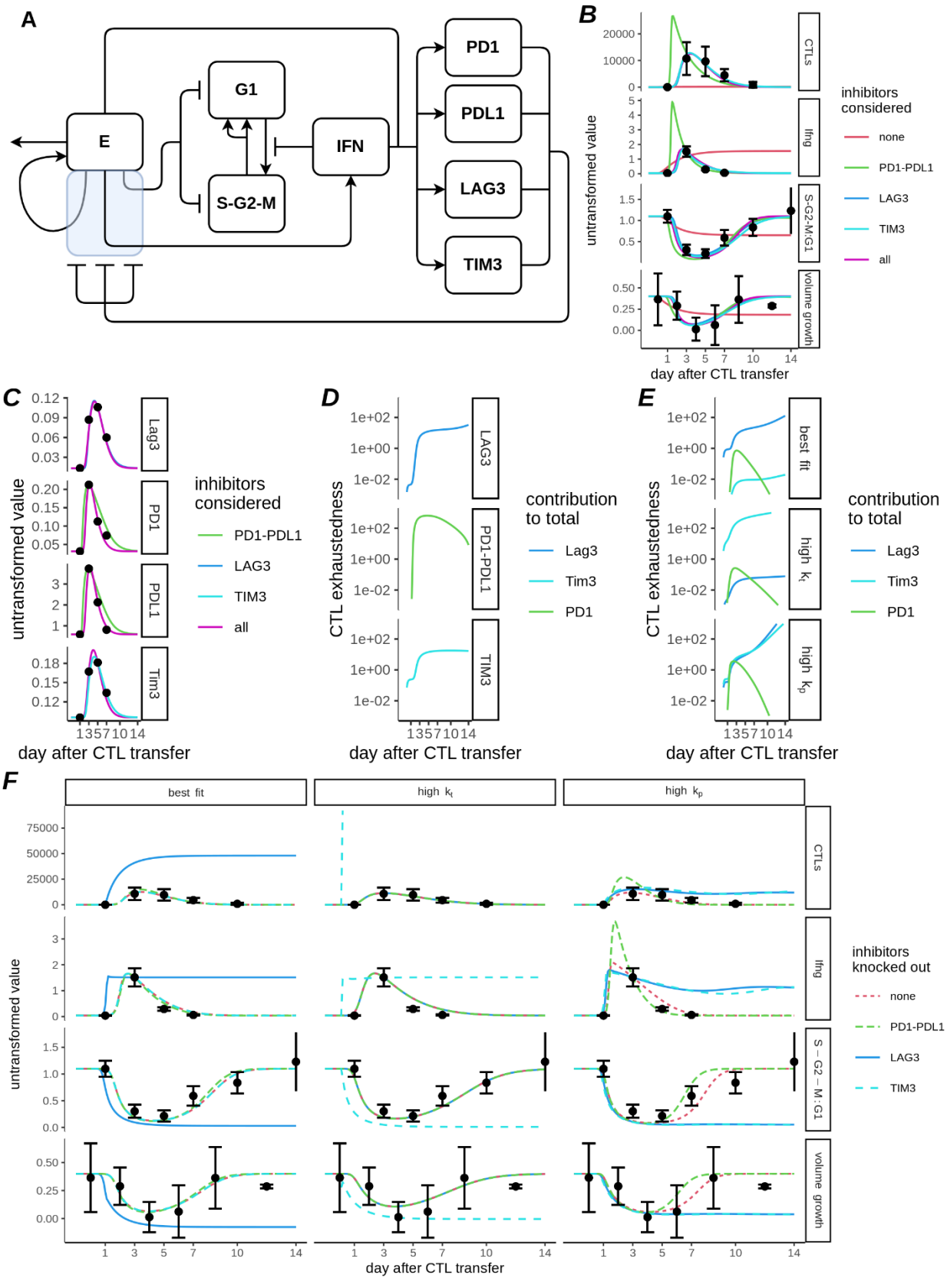
A
E
G1
S-G2-M
IFN
PD1
PDL1
LAG3
TIM3
B
CTLs
Ifng
S-G2-M:G1
volume growth
untransformed value
day after CTL transfer
inhibitors considered
none
PD1-PDL1
LAG3
TIM3
all
C
Lag3
PD1
PDL1
Tim3
untransformed value
day after CTL transfer
inhibitors considered
PD1-PDL1
LAG3
TIM3
all
D
LAG3
PD1-PDL1
TIM3
CTL exhaustedness
day after CTL transfer
contribution to total
Lag3
Tim3
PD1
E
best fit
high k_t
high k_p
CTL exhaustedness
day after CTL transfer
contribution to total
Lag3
Tim3
PD1
F
best fit
high k_t
high k_p
CTLs
Ifng
S−G2−M:G1
volume growth
untransformed value
day after CTL transfer
inhibitors knocked out
none
PD1-PDL1
LAG3
TIM3

Figure 5. (displayed on previous page) Early cessation of IFN-γ is quantitatively compatible with the development of CTL exhaustion. A) Schematic for ODE model of CTLs versus B16F10 melanoma. Pointed arrows represent a positive effect (i.e. transfer, production, recruitment), whilst flat-headed arrows represent an inhibiting effect. CTL functions that are reduced due to CTL exhaustion are represented by lines passing through the translucent blue box. B) Model fits to CTL density (top row), IFN-γ mRNA expression (2nd row), ratio of S-G_2-M:G_1 nuclei (3rd row), or volumetric tumour growth (bottom row). C) Model fit to ICs for each considered combination of ICs used for fitting the model. Different ICs are shown in each row as indicated by facet label. Colored lines in B-C represent model output, and model fits with different ICs are indicated by colour. D) CTL exhaustion level, when individual ICs were used to fit the model (as indicated in rows). Different coloured lines are the contribution for each term in Eq. 11 (see Methods), i.e: dark blue - $k_l L/E$; cyan - $k_h H/E$; green - $k_p(P/E)(P_L V/V_0)$. E) Contribution of different ICs to CTL exhaustion level, when all ICs were used to fit the model. Shown are results from the best fitting parameter set (top row), and two selected parameter sets with the highest contributions towards exhaustion from TIM-3 (middle row) or from PD-1/PD-L1 (bottom row). F) Results of knocking out individual inhibitors (as indicated by color and linetype) when all inhibitors were initially included in the fit: for either the best fitting model (column 1), the model with highest contribution from TIM-3 (column 2), or the model with highest contribution from PD-1/PD-L1 (column 3). In all panels, points and error bars represent (respectively) mean +/- s.d. of experimental data used to fit the model, and lines represent model simulations. Parameter values for best fitting models are given in Table 1.

Since our fitting procedure generated a range of parameter sets, we checked whether any of the other generated parameter sets might permit a larger role for TIM-3 or PD-1/PD-L1. To this end we selected the best fitting 20% of parameter sets amongst the final generation of our evolutionary algorithm, all of which resulted in reasonably good fits to the experimental data (Fig. S2). From this subset, we selected the parameter sets with either the highest value of k_t relative to the other exhaustion parameters or the highest relative value of k_p, i.e. the parameters which (respectively) controlled the contribution of TIM-3 and PD-1/PD-L1 towards exhaustion. The parameter set with a high value for k_t resulted in development of an exhausted state that was dominated by the contribution of TIM-3 (Fig. 5E, row 2), and knockout of TIM-3 in this model completely disrupted model dynamics (Fig. 5F, column 2). This supports the result from the individual fits because it shows that TIM-3, similarly to LAG-3, correlates well with the exhausted CTL state. The parameter set with a high value for k_p resulted in development of an exhausted state that had initially approximately equal contributions from all ICs, before PD-1/PD-L1 dropped and LAG-3 and TIM-3 took over the role as determinants of exhaustion (Fig. 5E, row 3). There, knockout of any of the ICs disrupted the dynamics of the model, although PD1/PD-L1 knockout led to disruption of early dynamics and LAG-3 or TIM-3 knockout to disruption of late dynamics (Fig. 5F, column 3). Overall, these results show that the brief window of IFN-γ production is quantitatively consistent with development of an exhausted state amongst CTLs, and that expression of the immune checkpoint molecules LAG-3 and TIM-3 correlate best with the development of this exhausted state. Our analysis suggests that of the three ICs considered, PD-1/PD-L1 is the least important determinant of the exhausted CTL state, however our model remains compatible with PD-1/PD-L1 playing a role in CTL exhaustion at early time points after CTL infiltration of the tumour.

Discussion

In a previous study on which our work was built, Matsushita et. al. found that tumour control of B16F10 melanoma by CTLs was mediated by a combination of cytotoxic and cytostatic effects, with the cytostatic effects being due to IFN-γ mediated cell cycle arrest of the melanoma cells[15]. However, the progression of cytostatic and antiproliferative effects over time was not explicitly explored. Here, we analysed image data, tumour volume measurements, and transcriptomics data from the study by Matsushita et. al[15], using data acquired at multiple timepoints after CTL transfer. We found that the presence of CTLs inside the tumour strongly correlated with tumour cell cycle arrest, as well as with the inhibition of volumetric tumour growth. However, IFN-γ signalling within the tumours followed early dynamics, with CTLs primarily producing IFN-γ early after arrival in the tumours. Since the loss of IFN-γ preceded the recovery of tumour cell proliferation, it was unclear whether IFN-γ signalling could completely account for the observed tumour cell cycle arrest, and what role T cell exhaustion had in these processes. Therefore, we developed an ODE model to describe tumour growth, CTL infiltration, CTL production of IFN-γ and subsequent interference with cell cycle progression, and also killing of tumour cells by CTLs. Using this model we were able to describe all the experimental data, which led us to conclude that IFN-γ mediated tumour cell cycle arrest, together with killing of tumour cells by CTLs, were sufficient mechanisms to account for the experimental data. We also used our models to compare the contribution of CTL mediated cytotoxic or cytostatic effects towards tumour control. Our model predicted CTL killing rates (k_e) between 0-3 CTL^{-1} day^{-1}, which resulted in only a minor contribution of CTL killing towards tumour control compared to the IFN-γ mediated cell cycle arrest, consistent with our findings from a B16F10 tumour we have previously analysed[19].

As part of our study, we developed a model describing the dynamics and effector functions of tumour infiltrating CTLs. Based on mRNA expression data, IFN-γ transcription peaked on day 3, had fallen sharply by day 5, and was virtually zero on day 7. This was in contrast to the number of CTLs which remained present in similar numbers on days 3 and 5, and were still observable in reasonable numbers at late time points. Therefore, our model required inclusion of the development of CTL exhaustion in order to account for this loss in ability to produce IFN-γ. CTL exhaustion is identified by a progressive increase in the number and diversity of inhibitory receptors expressed by CTLs[23,26,27]. We identified four well known inhibitory molecules amongst the available transcriptomics data: LAG-3, TIM-3, PD-1, and the PD-1 ligand PD-L1. With our model we were able to obtain good fits if the exhausted state was correlated with TIM-3 or LAG-3, but not with PD-1/PD-L1, which was due to the early peak of PD-1 and PD-L1 transcription that was already well in decline on day 5 whilst CTL numbers in the tumour remained high. This early peak was not compatible with the idea that CTLs were becoming gradually more exhausted over time. On the other hand, LAG-3 and TIM-3 increased relative to the CTLs over time and therefore correlated most with the loss of IFN-γ transcription. Consistent with our model prediction, LAG-3 and TIM-3 have been previously shown to have high correlation with dysfunctional “exhausted” phenotype in $CD8^+$ CTLs in melanoma[24]. Our model was not compatible with the dynamics of PD-1/PD-L1 as sole correlates of the exhausted state, which appears at first sight to contradict reports indicating that PD-1/PD-L1 signalling is relevant for immunosuppression in melanoma[28,29], although our result agrees with others showing the

B16F10 cell line in particular may be resistant to PD-1 antagonist monotherapy[30,31] . Since our model was compatible with PD-1/PD-L1 signalling making a partial contribution to CTL exhaustion at early time points, it may be that PD-L1/PD-1 plays only an initial role in immune suppression and that this role is taken over later by other checkpoints, which is consistent with findings that blockade of LAG-3 as well as PD-1 receptors is required to prevent relapse in melanoma[28]. One caveat for the data employed to fit our model is that only one probe was available per checkpoint. Therefore future experiments should confirm the dynamics of the expression of these immune checkpoint molecules and further investigate their contribution to T cell exhaustion.

Our model implies that the reduced activity of CTLs and in particular the apparent reduction in IFN-γ which preceded the disappearance of CTLs in the tumour by several days, could be explained by the development of an exhausted phenotype in the tumour infiltrating CTLs. Moreover, in our model IFN-γ played an important role in driving this exhausted phenotype. For exhaustion related to the PD-L1/PD-1 axis, this is clearly justified, because IFN-γ can induce upregulation of PD-L1 on tumour cells[13]. Moreover, IFN-γ induces increased antigen presentation on tumour cells[12], which should lead to increased stimulation of CTLs via their T cell receptors. This could explain the contribution of IFN-γ towards upregulation of the other immune checkpoints included in our model, which are more commonly associated with excessive and prolonged exposure to antigen[27]. In order to further study the dynamics of the CTL population in the tumour it would be useful to perform a second transfer of CTLs, which may help elucidate the extent to which the mechanisms of decline in CTL function are due to transferred CTLs becoming exhausted (and therefore a second transfer of “fresh” CTLs should result in similar anti-tumour effects) or are due to resistive mechanisms deployed by the tumour (in which case a second transfer of CTLs would be expected to provide only limited benefit).

Our study was limited by a lack of direct data concerning several important aspects of the CTL dynamics within the tumour. First, we had no direct data on the killing rate (k_e) of the CTLs inside the tumour, so this parameter was allowed to vary freely during the fitting process. Depending on which immune checkpoint molecules were included in the fitting process, we recovered a range of different values for k_e, although these parameters were all plausible and comparable with other values for the killing rate of tumour cells by CTLs *in vivo* reported elsewhere[32], including that for attack of B16F10 cells[19]. Importantly, however, the choice of immune checkpoint molecules and the resultant values of k_e did not impact our conclusion that IFN-γ mediated cell cycle arrest was the main determinant of tumour control. A second limitation surrounds our model of CTL exhaustion inside the tumours. Two specific questions we could not address due to the whole-tumour microarray data we used were: 1) which cells were expressing inhibitory molecules and 2) whether our results would have been different had we included ‘missing’ relevant molecules from the transcriptomics data, e.g. the immune checkpoint CTLA-4. Unbiased gene expression data generated at the single cell level, using single cell RNA-Seq techniques, would therefore be interesting to incorporate into similar modelling strategies in future. A third limitation is the possible presence of other tumour infiltrating cells, such as MDSCs which are recruited to B16F10 tumours after adoptive transfer of CTLs and exert suppressive effects on the tumour infiltrating CTLs[33]. The frequency of various immune cell types can be inferred from either single cell, or bulk transcriptomic data using computational methods[34], and it would be interesting to extend our modelling approach to include other relevant immune cells using such methods in future.

In our analysis, we used mRNA expression as a substitute for protein expression. Previous studies report that mRNA levels are substantially predictive of protein expression levels[35,36]. Moreover, although some delay should be expected between mRNA expression and protein expression, this delay has been estimated to last for only a few hours[36] and thus should not have a significant impact on our data, which consists of measurements made across several days. For the *in vivo* setting we studied, the rapid decline in the S-G_2-M : G_1 ratio after transfer of CTLs indeed suggests that protein expression rapidly follows mRNA expression. Conversely, the S-G_2-M : G_1 ratio does not appear to recover immediately upon downregulation of IFN-γ mRNA. One explanation could be that the effect of IFN-γ lasts longer than the protein due to downstream signaling. Another is that tumour cells are very sensitive to low levels of IFN-γ, therefore the effect could persist even after IFN-γ synthesis has substantially declined. The latter explanation seems to be in line with a study which found that bystander sensing of IFN-γ could occur at distances of over 40 cell lengths[13], implying high sensitivity of tumour cells to this cytokine.

In summary, we have presented a mathematical model that can successfully predict inhibition of tumour growth following adoptive T cell transfer. We used this model to quantify the contribution of IFN-γ and cytotoxicity to the antitumour activity of CTLs, which led to the conclusion that IFN-γ contributes most to tumour growth blockade by CTLs. Our model also includes anti-tumourigenic (antiproliferative, enhancing recruitment of CTLs) and pro-tumourigenic (driver of CTL exhaustion) effects of IFN-γ. The presence of opposing effects of IFN-γ have led to descriptions of an “IFN-γ paradox”[12]. Our model, by including these different effects associated with IFN-γ, can serve as a quantitative baseline to be augmented in future, and may help guide further experimental work.

Methods

Data Summary

For the development of the mathematical model, data from the paper by Matsushita et al.[15] were used. In brief, the experimental protocol in that previous study involved inoculation with 10^7 B16F10 melanoma cells into C57BL/6 mice, followed 9 days later by adoptive transfer of 10^6 activated pmel-1 transgenic T cells recognising the gp100 peptide (note that throughout the current study, the day of CTL transfer is designated “day 0”). The data included measurements of tumour volume from experiments in mice either with or without subsequent adoptive transfer of CTLs. From the same experiments we also used fluorescence microscope images of cryosections of B16F10 tumours expressing the fucci cell cycle sensor, taken on days 1,3,5,7,10 & 14 following CTL transfer. Finally, the data set included microarray RNA expression data from B16F10 tumours at days 1, 3, 5 & 7 after CTL transfer.

Image analysis

Automated estimates of the number of G_1 or S-G_2-M phase nuclei were produced using the ilastik (version 1.1.3) cell density estimation tool. Training and classification was performed using merged (RGB) images. For training the classifier we selected subregions (100-200μm^2) from the larger (750x550μm) cryosections. One subregion was selected from each available time point to

ensure a representative training set. Pipelines for different nuclei (G_1 or S-G_2-M) were trained separately. Training was performed by manually labelling training images until the classifier estimated numbers of cells achieved a satisfactory match with manual counts for the same data.

Analysis of gene expression data

Microarray data were downloaded from the Gene Expression Omnibus (GEO) database (series GSE57304; samples GSM1379331– GSM1379344). These data correspond to the same set of experiments as the image and tumour volume progression data we have used, and the methodology for acquisition of these data has been described previously[15]. Briefly, tumour tissues from mice were harvested on different days (1,3,5,7) after CTL transfer, or on the same days in the untreated (without CTLs) condition. Each sample contained 500ng of pooled RNA from 3-4 different tumours, and microarray analysis was performed with 45,018 probes to quantify expression levels of the targeted genes. We performed similar data processing steps to the original publication: probes were discarded when their gIsWellAboveBG flag was zero at all samples, and we normalised different samples at the 75th percentile.

Basic ODE Model

We developed an ODE model to describe the intratumoral activities of the transferred CTLs. The basic model of tumour growth (in the absence of CTLs) considers two possible states for alive tumour cells: they can be either in the G_1 phase of the cell cycle (denoted in the equation as G), or else in the S, G_2, or M phase (together denoted S in the model equations). The reason for choosing these states as explicit model variables was because the Fucci cell cycle reporter used in the experiments, which our model is based upon, could distinguish only between G_1 or S-G_2-M phases. Cells move from the G_1 state into the S-G_2-M state at rate k_{gs}, and leave the S-G_2-M state at rate k_{sg} (Eq. 1):

$$\frac{dS}{dt} = k_{gs}G - k_{sg}S. \qquad \text{Eq 1}$$

The S-G_2-M state concludes when a tumour cell undergoes mitosis. To include this increase in tumour cells in our model, we consider that for every cell which leaves the S-G_2-M state, two cells enter the G_1 state (Eq 2):

$$\frac{dG}{dt} = -k_{gs}G + 2k_{sg}S. \qquad \text{Eq 2}$$

The resulting tumours grow exponentially when the ratio of cells in G and S states is at its steady state value. When CTLs (*E*) are introduced into the tumours, our basal model of tumour growth (Eq's 1-2) is modified to include two possible effects CTLs can have on the tumour. The first of these effects is direct killing of tumour cells, which occurs with a constant rate k_e (per CTL). As

we have done previously[18,19], we take the total killing activity of CTLs to be directly proportional to the number of CTLs inside the tumour, such that the total killing activity of the CTLs is given by $\alpha k_e E$ (note that $\alpha$is a scalar used to modify the effector functions of CTLs if their activity is reduced due to being exhausted: see Eq's 7-12). We consider that killing is directed equally towards cells in G_1 or S-G_2-M phases, so that the fraction of tumour cells in either state (i.e. $G\ (S+G)^{-1}$ or $S\ (S+G)^{-1}$, respectively) determines the fraction of the total killing activity that each subset of tumour cells receives.

The second effect that CTLs can have on the tumour is an antiproliferative effect, mediated by IFN-γ, which results in an arrest of the cell cycle in the G_1 phase. To include this effect in our model we reduce the transition of cells out of the G_1 phase by scaling with the term $(1+k_i I/V)^{-1}$. Here, the variable I represents the total quantity of IFN-γ inside the tumour and V is the variable representing tumour volume. Thus, the term I / V represents the concentration of IFN-γ inside the tumours, and k_i determines the concentration dependence of the IFN-γ dependent reduction in the rate at which tumour cells can leave the G_1 phase. The equations to describe the evolution of the number of tumour cells in G_1 or S-G_2-M phases become:

$$\frac{dS}{dt} = k_{gs} G\ (1+k_i I/V)^{-1} - k_{sg} S - \alpha k_e\ E\ S\ (S+G)^{-1}, \qquad \text{Eq 3}$$

$$\frac{dG}{dt} = -k_{gs} G\ (1+k_i I/V)^{-1} + 2k_{sg} \cdot S - \alpha k_e\ E\ G\ (S+G)^{-1}. \qquad \text{Eq 4}$$

To test the compatibility of IFN-γ transcription dynamics with G_1 tumour cell cycle arrest Eq's 3-4 were used directly. *I* and *E* were estimated by linearly interpolating between the mean of the experimental data at each available time point, and these linear interpolations were used as inputs to the model.

ODE Model with CTL dynamics

To describe the dynamics of the CTL population and their production of IFN-γ, we extended our basic ODE model with further equations. We consider that after transfer, CTLs would begin to arrive in any given region of the tumour at a constant rate s_0. We take a constant rate of CTL arrival per unit volume of tumour, hence the rate at which CTLs can find the tumour scales with tumour volume. Moreover, we consider that CTLs expand within the tumour at rate s_e, and die at a constant rate, d_E. CTL expansion inside the tumour is also reduced according to the level of CTL exhaustion (α). Thus, CTL dynamics is described by the following equation:

$$\frac{dE}{dt} = s_0 V + \alpha s_e E - d_E E. \qquad \text{Eq 5}$$

We consider CTLs to be the major source of IFN-γ inside the tumours, therefore IFN-γ production is proportional to the number of CTLs, but is reduced according to their level of exhaustion (α), and IFN-γ disappears from the system with a rate d_i:

$$\frac{dI}{dt} = \alpha E - d_i I. \quad \text{Eq 6}$$

Finally, we include a mechanism whereby CTLs become exhausted inside the tumour. T cell exhaustion is characterised by a loss of effector functions along with a progressive increase in the amount and diversity of inhibitory receptors expressed by T cells[23,26,27]. We used the well described PD1, PD-L1, LAG-3 & TIM-3 inhibitory molecules as indicators of exhausted T cells[24], which in our model appear with variable names P, P_L, L, and H (respectively):

$$\frac{dP}{dt} = E(1 + k_A I/V) - d_p P, \quad \text{Eq 7}$$

$$\frac{dP_L}{dt} = E(1 + k_A I/V) - d_{pl} P_L, \quad \text{Eq 8}$$

$$\frac{dL}{dt} = E(1 + k_A I/V) - d_l L, \quad \text{Eq 9}$$

$$\frac{dH}{dt} = E(1 + k_A I/V) - d_t H. \quad \text{Eq 10}$$

We tested several model variants, one with no immune checkpoints, three in which we consider one checkpoint at a time, and one considering all checkpoints simultaneously. All inhibitory molecules follow similar dynamics, increasing in proportion to the number of CTLs inside the tumour and disappearing from the system with different rate constants d_p,d_{pl},d_l, and d_t (respectively). Production is increased proportional to the term $(1 + k_A I/V)$, which allows for a contribution of IFN-γ to the exhausted state. Note that the IFN-γ induction of exhaustion may be direct or indirect, e.g. by increasing antigenicity of tumour cells and thereby increasing stimulation of T cells via the T cell receptor. In our model, we consider PD1, LAG-3, and HAVCR2 as expressed on the membrane of CTLs, so the ratio of each of these checkpoint molecules to the number of CTLs determines the overall level of exhaustion of the CTLs in our model. PDL1 is modelled differently, being a ligand for the PD1 receptor, and the concentration of PDL1 in our model is multiplied together with the membrane density of PD1 expressed on CTLs to determine

the contribution from PD1-PDL1 signalling (see Eq. 11 in ref: [37]). To describe the joint effect of these inhibitory molecules on the CTLs, we consider a weighted sum *R*:

$$R = k_l L/E + k_t H/E + k_p (P/E)(P_L/V). \quad \text{Eq 11}$$

R represents the total "exhaustedness" of the CTL population inside the tumour. The parameters k_l, k_t, and k_p represent the individual contribution of (respectively) LAG-3, TIM-3, and PD-1/PD-L1 signalling towards the level of exhaustion of CTLs. In absence of detailed information about the impact of exhaustion level on CTL functions (killing, IFN-γ production, expansion), we take all these functions to be equally reduced with the level of CTL exhaustion:

$$\alpha = 1 - (1 + k_{ex}/R)^{-1}. \quad \text{Eq 12}$$

Here, k_{ex} is the level of exhaustion at which all effector functions are half of their maximum value. Thus, Equation 12 scales the exhaustion level to a scaled term α which can range from 0 to 1 and is applied to the relevant rate constants in Equations 3-6.

Parameter estimation

Parameter estimation for the two parameters in the basal tumour growth model was performed separately from the other parameters. We consider that the density of the tumour cells remained constant over time, so that volumetric tumour growth rate could be taken as a proxy for the expansion rate of the tumour cell population. We obtained an estimate for the untreated tumour growth rate (*g*) from fitting an exponential model of tumour growth to the volumetric growth data for the untreated tumours. Moreover, estimates of the ratio of tumour cells in the S-G_2-M : G_1 phase gave a second measurement allowing the two parameter (k_{gs}, k_{sg}) basal model of tumour growth to be completely defined, considering that the ratio of S-G_2-M : G_1 phase tumour cells has reached a steady state (which is reasonable since we deal with data two weeks after tumour inoculation). Then, using the equation for exponential growth:

$$\frac{d(S+G)}{dt} = g\,(S + G), \quad \text{Eq 13}$$

where g is the tumour growth rate, one can substitute the left hand side of Eq.13 with $k_{sg}S$, noting that $k_{sg}S$is the total rate of new tumour cell production obtained from summing Eq's. 1-2. Following the substitution, an expression for *g* can be found in terms of S and G:

$$g = k_{sg} S \,/\, (S + G). \qquad \text{Eq 14}$$

Since our model results in an exponentially growing tumour with a constant ratio of cells in S:G states, explicit equations for the growth of the populations in each state can be written separately:

$$S(t) = S_{ss} e^{gt}, \qquad \text{Eq 15}$$

$$G(t) = G_{ss} e^{gt}, \qquad \text{Eq 16}$$

with the subscript (SS) indicating validity of these equations when the initial populations are at their steady state ratio. Following differentiation of each equation:

$$\frac{dS}{dt} = g S_{ss} e^{gt}, \qquad \text{Eq 17}$$

$$\frac{dG}{dt} = g G_{ss} e^{gt}, \qquad \text{Eq 18}$$

the resulting equations (17-18) can be combined to remove the common terms ($g e^{gt}$). This leads to the following:

$$\frac{1}{S}\frac{dS}{dt} = \frac{1}{G}\frac{dG}{dt}, \qquad \text{Eq 19}$$

where we have omitted the subscript with the understanding that Eq. 19 is valid only when the tumour is growing exponentially with the ratio S/G at a steady state value. Therefore, by substituting the expressions for $\frac{dG}{dt}$ and $\frac{dS}{dt}$ given in Eq's 1-2, the Eq's 14 & 19 can be rearranged to express the k_{sg} and k_{gs} parameters for the basal tumour growth model as a function of tumour growth rate (g) and the ratio of S-G_2-M : G_1 phase tumour cells at steady state:

$$k_{sg} = g\,(1 + S/G)(S/G)^{-1}, \qquad \text{Eq 20}$$

$$k_{gs} = g\,(1 + 2S/G).$$ Eq 21

The remaining model parameters which relate to the dynamics of the CTLs and their effects on the tumours were obtained together, by fitting to all available data over time simultaneously (i.e. the CTL counts; the S/G ratios; the volumetric growth data; the IFN-γ expression data; the immune checkpoint expression data). The measurements derived from the experimental data are multivariate and do not have the same dimension or scale. To avoid the set of measurements with the largest numerical values from dominating the fit, we could not easily use studentized residuals (i.e. dividing residuals by the estimated standard deviation of the measurements) to remove the dimensionality of each measurement, because for a number of experimental observations (CTLs on day 1, all immune checkpoints) the estimated standard deviation would be zero. Instead, we opted to apply Min-Max feature scaling. For a given set of experimental measurements of the same type denoted X (where X could be, for example, the number of CTLs counted on each different day of measurement), the equation for the transform is given by the following:

$$X_s = (X - min(X))/(max(X) - min(X)),$$ Eq 22

where $X_s$is the set of Min-Max rescaled measurements and min(X) and max(X) are the smallest and largest values for the subset of experimental data under consideration. Thus, all experimental data is linearly rescaled to the range between 0-1. The same transformation is applied to the measurements sampled from the model,

$$Y_s = (Y - min(X))/(max(X) - min(X)).$$ Eq 23

Note that the model output is scaled relative to the experimental data, thus rescaled values for modelled variables are allowed to take values outside the range 0-1. Finally, the root-mean-square error (RMSE) is calculated:

$$RMSE = \sqrt{\frac{\sum^{n} (x_n - y_n)^2}{n}},$$ Eq 24

where n is the total number of measurement points used in the fitting and xn and yn are the individual measurements taken from the experimental data and the model output, respectively. After fitting the reverse calculation is applied to convert back to the original scaling for the

experimental data. For the basic model with I and E used as inputs, there were only two parameters (ki and ke) to be estimated, therefore we tested all combinations of the parameters in the range 0-20 at intervals of 0.1 and selected the combination with the lowest RMSE. For the model including CTL dynamics we used an evolutionary algorithm[38] to minimise the RMSE, following the local-to-best strategy, with a population size of 500 and lasting for 1500 generations. Best-fitting parameter sets are provided in Table 1.

Table 1. Description of model parameters, with best fitting parameter values. Columns 2-4 give values for ICs fit individually, columns 5-7 give values for fits with all ICs included.

symbol	Best (LAG)	Best (TIM)	Best (PD)	Best (all)	Best (all-high k_t)	Best(all-high k_p)	Units	Description
s_0	0.011	0.087	0.007	0.032	0.04	0.008	(mm^{-3} day^{-1})	Infiltration rate of CTLs into tumour
s_e	8.39	9.10	13.56	14.97	116	17.97	(day^{-1})	Expansion rate of CTL population within tumour
d_e	0.91	0.89	0.47	1.19	0.4	1.23	(day^{-1})	Death rate of CTLs inside tumour
d_i	4.74	3.87	0.80	25.1	1.06	10.1	(day^{-1})	Rate at which IFN-γ disappears from the system.
k_{gs}	1.64						(day^{-1})	Basal tumour cell transition rate from G_1 to S-G_2-M cell cycle phases
k_{sg}	0.66						(day^{-1})	Basal tumour cell transition rate from S-G_2-M to G_1 cell cycle phase
k_i	0.011	0.035	0.063	0.038	0.18	0.35	(IFN^{-1} mm^3)	Determines the concentration of IFN-γ required to prevent transfer of tumour cells from G_1 to S-G_2-M cell cycle phases. k_i^{-1} is the concentration of IFN-γ required to reduce the transition rate by 50%.
k_e	3.57	4.20	0.007	2.72	1.44	0.007	(CTL^{-1} day^{-1})	Rate at which CTLs kill tumour cells
k_A	0.69	0.013	0.011	0.025	0.016	0.012	(IFN^{-1} mm^3)	Relative contribution of IFN-γ to immune checkpoint expression
k_{ex}	22.4	28.9	13.6	7.92	0.9	0.067	CTL^{-1}	Determines level of immune checkpoint expression required to decrease CTL function
k_l	0.78	NA	NA	52.5	0.02	0.13	(LAG^{-1})	Contribution of LAG3 towards CTL exhaustion
k_t	NA	48.6	NA	0.043	104	0.21	(TIM^{-1})	Contribution of TIM3 towards CTL exhaustion
k_p	NA	NA	0.007	0.10	0.009	0.01	($PD1^{-1}$ $PDL1^{-1}$ mm^3)	Contribution of PD-1/PD-L1 towards CTL exhaustion
d_l	0.41	NA	NA	0.74	0.053	0.37	(day^{-1})	Disappearance rate of LAG3 inside the system
d_t	NA	0.51	NA	1.18	0.3	0.57	(day^{-1})	Disappearance rate of TIM3 inside the system
d_p	NA	NA	0.22	67.3	13.7	125	(day^{-1})	Disappearance rate of PD-1 inside the system
d_{pl}	NA	NA	0.26	15.1	116	20.4	(day^{-1})	Disappearance rate of PD-L1 inside the system

References

1. Tang J, Pearce L, O'Donnell-Tormey J, Hubbard-Lucey VM. Trends in the global immuno-oncology landscape. Nat Rev Drug Discov. 2018;17: 783–784.

2. Liu Y, Bewersdorf JP, Stahl M, Zeidan AM. Immunotherapy in acute myeloid leukemia and myelodysplastic syndromes: The dawn of a new era? Blood Rev. 2019;34: 67–83.

3. Nixon NA, Blais N, Ernst S, Kollmannsberger C, Bebb G, Butler M, et al. Current landscape of immunotherapy in the treatment of solid tumours, with future opportunities and challenges. Curr Oncol. 2018;25: e373–e384.

4. Gibney GT, Weiner LM, Atkins MB. Predictive biomarkers for checkpoint inhibitor-based immunotherapy. Lancet Oncol. 2016;17: e542–e551.

5. Ribba B, Boetsch C, Nayak T, Grimm HP, Charo J, Evers S, et al. Prediction of the Optimal Dosing Regimen Using a Mathematical Model of Tumor Uptake for Immunocytokine-Based Cancer Immunotherapy. Clin Cancer Res. 2018;24: 3325–3333.

6. Qomlaqi M, Bahrami F, Ajami M, Hajati J. An extended mathematical model of tumor growth and its interaction with the immune system, to be used for developing an optimized immunotherapy treatment protocol. Math Biosci. 2017;292: 1–9.

7. Melero I, Berman DM, Aznar MA, Korman AJ, Pérez Gracia JL, Haanen J. Evolving synergistic combinations of targeted immunotherapies to combat cancer. Nat Rev Cancer. 2015;15: 457–472.

8. Sharpe AH, Pauken KE. The diverse functions of the PD1 inhibitory pathway. Nat Rev Immunol. 2018;18: 153–167.

9. Salmaninejad A, Valilou SF, Shabgah AG, Aslani S, Alimardani M, Pasdar A, et al. PD-1/PD-L1 pathway: Basic biology and role in cancer immunotherapy. J Cell Physiol. 2019;234: 16824–16837.

10. Hegde UP, Mukherji B. Current status of chimeric antigen receptor engineered T cell-based and immune checkpoint blockade-based cancer immunotherapies. Cancer Immunol Immunother. 2017;66: 1113–1121.

11. Cazaux M, Grandjean CL, Lemaître F, Garcia Z, Beck RJ, Milo I, et al. Single-cell imaging of CAR T cell activity in vivo reveals extensive functional and anatomical heterogeneity. J Exp Med. 2019;216: 1038–1049.

12. Zaidi MR. The Interferon-Gamma Paradox in Cancer. J Interferon Cytokine Res. 2019;39: 30–38.

13. Hoekstra ME, Bornes L, Dijkgraaf FE, Philips D, Pardieck IN, Toebes M, et al. Long-distance modulation of bystander tumor cells by CD8+ T-cell-secreted IFN-γ. Nature Cancer. 2020;1: 291–301.

14. Garcia-Diaz A, Shin DS, Moreno BH, Saco J, Escuin-Ordinas H, Rodriguez GA, et al. Interferon Receptor Signaling Pathways Regulating PD-L1 and PD-L2 Expression. Cell Rep. 2017;19: 1189–1201.

15. Matsushita H, Hosoi A, Ueha S, Abe J, Fujieda N, Tomura M, et al. Cytotoxic T lymphocytes block tumor growth both by lytic activity and IFNγ-dependent cell-cycle arrest. Cancer Immunol Res. 2015;3: 26–36.

16. Harvat BL, Seth P, Jetten AM. The role of p27Kip1 in gamma interferon-mediated growth arrest of mammary epithelial cells and related defects in mammary carcinoma cells. Oncogene. 1997;14: 2111–2122.

17. Chin YE, Kitagawa M, Su WC, You ZH, Iwamoto Y, Fu XY. Cell growth arrest and induction of cyclin-dependent kinase inhibitor p21 WAF1/CIP1 mediated by STAT1. Science. 1996;272: 719–722.

18. Beck RJ, Slagter M, Beltman JB. Contact-Dependent Killing by Cytotoxic T Lymphocytes Is Insufficient for EL4 Tumor Regression In Vivo. Cancer Res. 2019;79: 3406–3416.

19. Beck RJ, Weigelin B, Beltman JB. CD137-stimulated cytotoxic T lymphocytes exert superior tumour control due to an enhanced antimitotic effect on tumour cells. bioRxiv. 2020. p. 2020.12.15.411538. doi:10.1101/2020.12.15.411538

20. Berg S, Kutra D, Kroeger T, Straehle CN, Kausler BX, Haubold C, et al. ilastik: interactive machine learning for (bio)image analysis. Nat Methods. 2019;16: 1226–1232.

21. Morris R, Kershaw NJ, Babon JJ. The molecular details of cytokine signaling via the JAK/STAT pathway. Protein Sci. 2018;27: 1984–2009.

22. Thommen DS, Schumacher TN. T Cell Dysfunction in Cancer. Cancer Cell. 2018;33: 547–562.

23. Wherry EJ. T cell exhaustion. Nat Immunol. 2011;12: 492–499.

24. Li H, van der Leun AM, Yofe I, Lubling Y, Gelbard-Solodkin D, van Akkooi ACJ, et al. Dysfunctional CD8 T Cells Form a Proliferative, Dynamically Regulated Compartment within Human Melanoma. Cell. 2019;176: 775–789.e18.

25. Singer M, Wang C, Cong L, Marjanovic ND, Kowalczyk MS, Zhang H, et al. A Distinct Gene Module for Dysfunction Uncoupled from Activation in Tumor-Infiltrating T Cells. Cell. 2016;166: 1500–1511.e9.

26. Blank CU, Haining WN, Held W, Hogan PG, Kallies A, Lugli E, et al. Defining “T cell exhaustion.” Nat Rev Immunol. 2019;19: 665–674.

27. Wherry EJ, Kurachi M. Molecular and cellular insights into T cell exhaustion. Nat Rev Immunol. 2015;15: 486–499.

28. Goding SR, Wilson KA, Xie Y, Harris KM, Baxi A, Akpinarli A, et al. Restoring immune function of tumor-specific CD4+ T cells during recurrence of melanoma. J Immunol. 2013;190: 4899–4909.

29. Hu Z, Ye L, Xing Y, Hu J, Xi T. Combined SEP and anti-PD-L1 antibody produces a synergistic antitumor effect in B16-F10 melanoma-bearing mice. Sci Rep. 2018;8: 217.

30. Chen S, Lee L-F, Fisher TS, Jessen B, Elliott M, Evering W, et al. Combination of 4-1BB agonist and PD-1 antagonist promotes antitumor effector/memory CD8 T cells in a poorly immunogenic tumor model. Cancer Immunol Res. 2015;3: 149–160.

31. Garris CS, Arlauckas SP, Kohler RH, Trefny MP, Garren S, Piot C, et al. Successful Anti-PD-1 Cancer Immunotherapy Requires T Cell-Dendritic Cell Crosstalk Involving the Cytokines IFN-γ and IL-12. Immunity. 2018;49: 1148–1161.e7.

32. Breart B, Lemaître F, Celli S, Bousso P. Two-photon imaging of intratumoral CD8+ T cell cytotoxic activity during adoptive T cell therapy in mice. J Clin Invest. 2008;118: 1390–1397.

33. Hosoi A, Matsushita H, Shimizu K, Fujii S-I, Ueha S, Abe J, et al. Adoptive cytotoxic T lymphocyte therapy triggers a counter-regulatory immunosuppressive mechanism via recruitment of myeloid-derived suppressor cells. Int J Cancer. 2014;134: 1810–1822.

34. Chen B, Khodadoust MS, Liu CL, Newman AM, Alizadeh AA. Profiling Tumor Infiltrating Immune Cells with CIBERSORT. Methods Mol Biol. 2018;1711: 243–259.

35. Guo Y, Xiao P, Lei S, Deng F, Xiao GG, Liu Y, et al. How is mRNA expression predictive for protein expression? A correlation study on human circulating monocytes. Acta Biochim Biophys Sin . 2008;40: 426–436.

36. Liu Y, Beyer A, Aebersold R. On the Dependency of Cellular Protein Levels on mRNA Abundance. Cell. 2016;165: 535–550.

37. Lai X, Friedman A. Combination therapy of cancer with cancer vaccine and immune checkpoint inhibitors: A mathematical model. PLoS One. 2017;12: e0178479.

38. Mullen K, Ardia D, Gil DL, Windover D, Cline J. DEoptim: An R Package for Global Optimization by Differential Evolution. 2009. Available: https://papers.ssrn.com/abstract=1526466

Supplementary Data

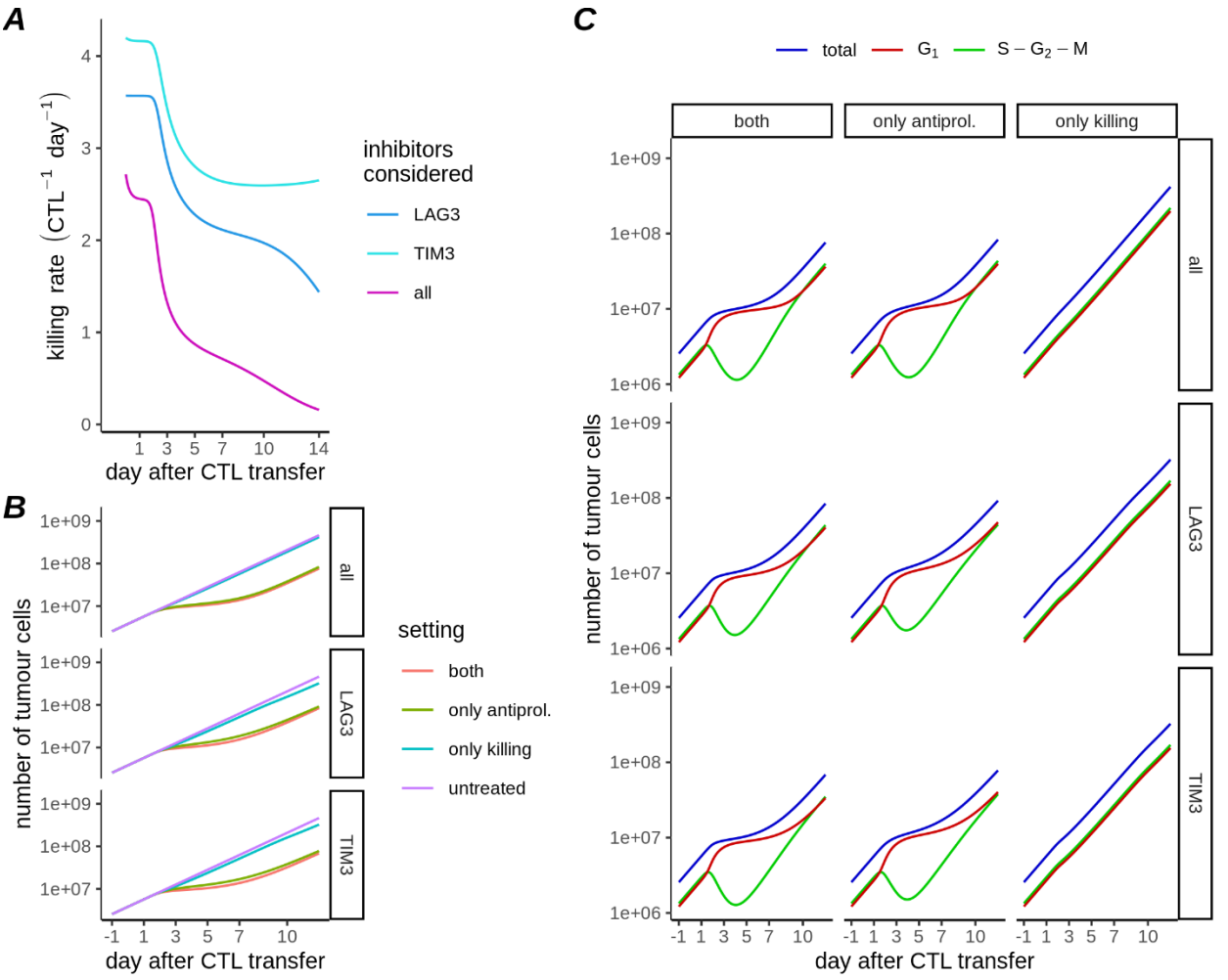

Figure S1. Relative effects of killing and IFN-γ in the fitted models. A) Different CTL killing rates predicted using the best fits for three IC combination models (only LAG-3, only TIM-3, or the combination of LAG-3, TIM-3 and PD-1/PD-L1), each of which resulted in a good fit to the experimental data. Each fitted combination is represented by a different color. B) Comparison of the number of tumour cells, predicted over time for each of the three selected IC combinations (along rows). Total cells (blue), G_1 phase cells (red), or S-G_2-M phases (green) are shown separately for each condition. Along columns are simulations with either all parameters as fitted (left), with killing disabled (middle), or with the antiproliferative effect disabled (right). C) Comparison of total number of tumour cells in the model for the 9 conditions simulated in B. An additional line ("untreated", purple) shows the growth of the tumour simulated without any CTLs.

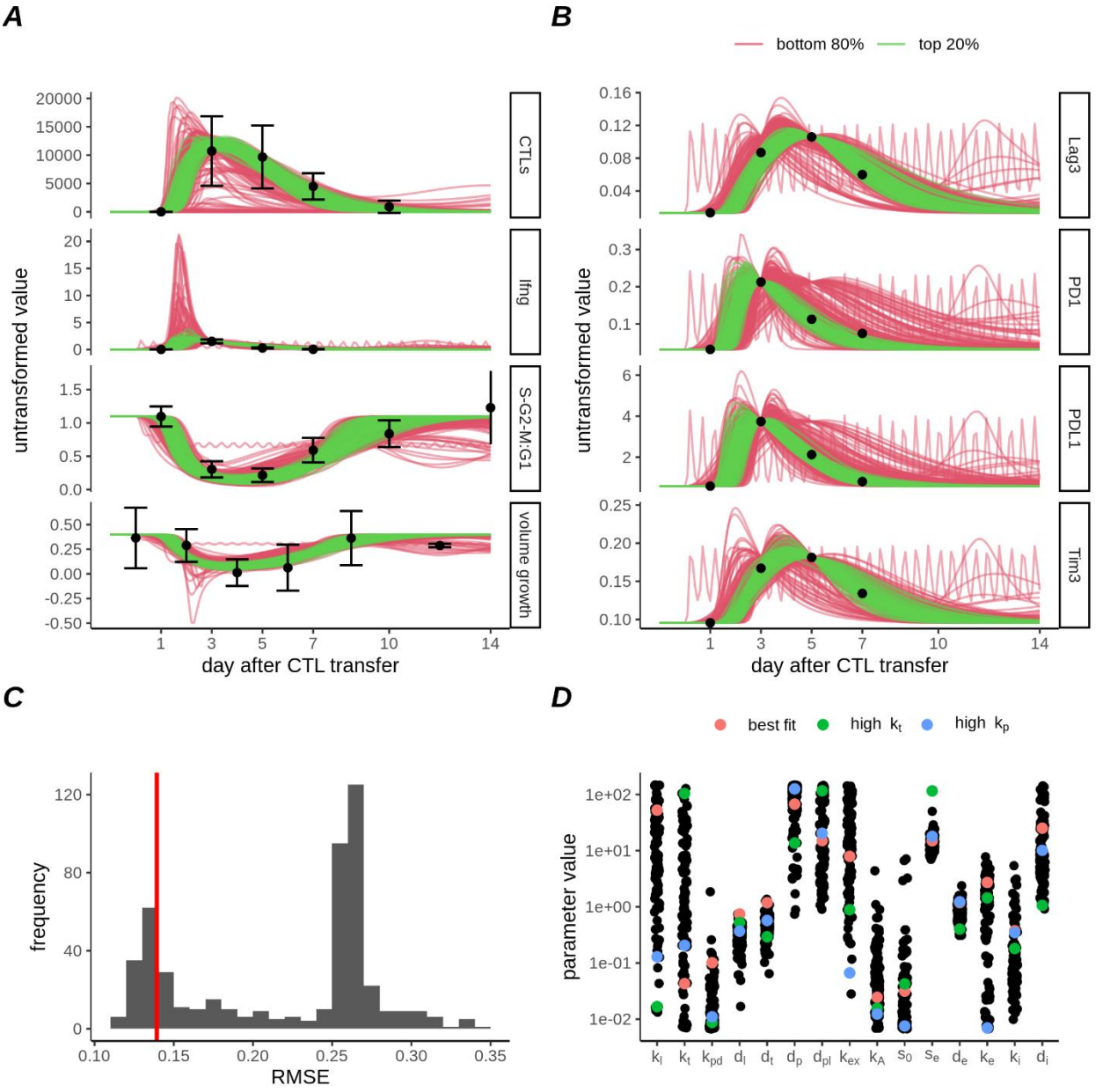

Figure S2. Parameter variability amongst the final generation of the evolutionary algorithm, when all ICs were used to fit the model. A) Model fits to CTL density (top row), IFN-γ mRNA expression (2nd row), ratio of S-G_2-M:G_1 nuclei (3rd row), or volumetric tumour growth (bottom row). B) Model fit to each IC as indicated by facet labels per row. Symbols and error bars in A-B represent experimental measurements and SD, whereas lines represent model output, and are coloured according to whether they were in the top 20% of the best fitting parameter sets. C) Distribution of root-mean-square-error (RMSE) for parameter sets in the final generation. Red line indicates the cutoff for the top 20% of parameter sets. D) Parameter values for the top 20% of parameter sets in the final generation of the evolutionary algorithm. Coloured dots indicate parameter sets for best fit (red) and for high relative values of k_t (green) and of k_p (blue) compared to other exhaustion parameters (these sets are used in Fig. 5E-F in main text).